AIP Journal of Applied Physics

# Coherent femtosecond low-energy single-electron pulses for time-resolved diffraction and imaging: A numerical study

A. Paarmann, M. Gulde, M. Müller, S. Schäfer, S. Schweda, M. Maiti, C. Xu, T. Hohage, F. Schenk, C. Ropers, and R. Ernstorfer

Citation: Journal of Applied Physics **112**, 113109 (2012); doi: 10.1063/1.4768204
View online: http://dx.doi.org/10.1063/1.4768204
View Table of Contents: http://scitation.aip.org/content/aip/journal/jap/112/11?ver=pdfcov
Published by the AIP Publishing



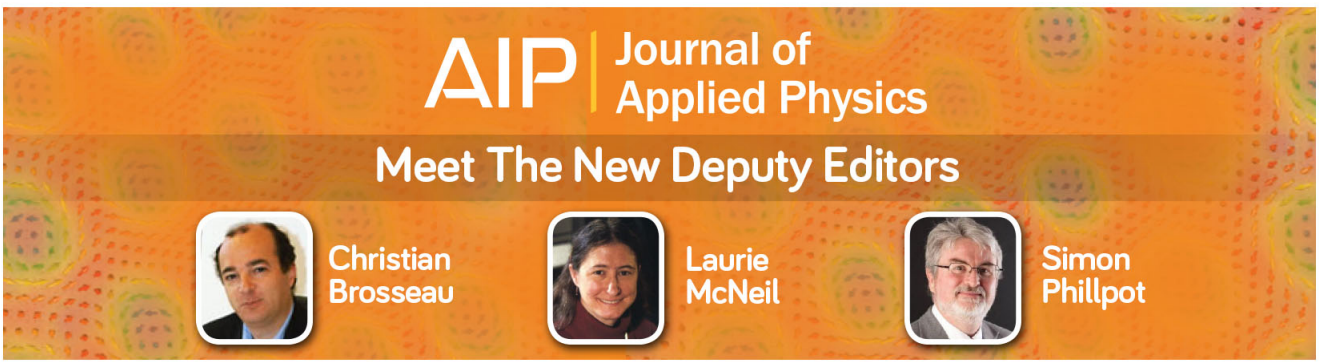

# Coherent femtosecond low-energy single-electron pulses for time-resolved diffraction and imaging: A numerical study

A. Paarmann,[1,a)] M. Gulde,[2] M. Müller,[1] S. Schäfer,[2,b)] S. Schweda,[2] M. Maiti,[2] C. Xu,[1,3] T. Hohage,[4] F. Schenk,[2,4] C. Ropers,[2] and R. Ernstorfer[1]
[1]*Fritz-Haber-Institut der Max-Planck-Gesellschaft, Faradayweg 4-6, 14195 Berlin, Germany*
[2]*Courant Research Center Physics & Material Physics Institute, University of Göttingen, Friedrich-Hund-Platz 1, 37077 Göttingen, Germany*
[3]*Shanghai Institute of Optics and Fine Mechanics, Chinese Academy of Science, 390, Qinghe Road, Jiading, Shanghai 201800, China*
[4]*Institute of Numerical and Applied Mathematics, University of Göttingen, Lotzestr. 16-18, 37083 Göttingen, Germany*

(Received 16 August 2012; accepted 31 October 2012; published online 10 December 2012)

We numerically investigate the properties of coherent femtosecond single electron wave packets photoemitted from nanotips in view of their application in ultrafast electron diffraction and non-destructive imaging with low-energy electrons. For two different geometries, we analyze the temporal and spatial broadening during propagation from the needle emitter to an anode, identifying the experimental parameters and challenges for realizing femtosecond time resolution. The simple tip-anode geometry is most versatile and allows for electron pulses of several ten of femtosecond duration using a very compact experimental design, however, providing very limited control over the electron beam collimation. A more sophisticated geometry comprising a suppressor-extractor electrostatic unit and a lens, similar to typical field emission electron microscope optics, is also investigated, allowing full control over the beam parameters. Using such a design, we find ~230 fs pulses feasible in a focused electron beam. The main limitation to achieve sub-hundred femtosecond time resolution is the typical size of such a device, and we suggest the implementation of more compact electron optics for optimal performance. © *2012 American Institute of Physics*. [http://dx.doi.org/10.1063/1.4768204]

## I. INTRODUCTION

Recently, there has been tremendous progress in ultrafast diffraction techniques,[1–5] allowing for the study of ultrafast dynamics of the atomic structure in crystalline solids and at surfaces. In these experiments, the diffraction of short X-ray or electron pulses is used as a delayed structural probe after femtosecond (fs) optical excitation of a sample. These studies can provide direct structural information with sub-Å spatial resolution and fs-temporal resolution.[1] The defining technological advances for this progress are sources of short X-ray or electron pulses. Sub-picosecond X-ray pulses can be produced from table-top plasma sources,[2] or by slicing of synchrotron electron bunches,[3] and are entering a new regime of brightness using X-ray free electron lasers.[4]

At the same time, the advent of femtosecond (fs) electron sources enabled a variety of ultrafast time-resolved experiments employing fs electron pulses, which besides ultrafast electron diffraction (UED)[1,5] also encompasses ultrafast microscopy.[6–8] In ultrafast diffraction, the use of an electron probe pulse has intrinsic advantages compared with X-rays in reduced radiation damage and better matching of the penetration depth of pump and probe pulses.[9] However, the temporal broadening of electron pulses due to electron-electron repulsion and velocity dispersion during propagation to the sample has been a big challenge.[10]

Up to now, most of the UED experiments employed flat photocathodes irradiated with intense fs-laser pulses at kHz repetition rates,[9] producing electron pulses containing 100 up to several 10 000 electrons. These conditions warrant sub-picosecond pulse durations for acceleration to several tens of keV and propagation of a few centimeters, allowing for the implementation of electron optics in the beam path.[9] More recently, radio frequency (rf) electron pulse compression down to 100 fs was demonstrated to allow for longer propagation for ~100 keV electron bunches.[11,12] Alternatively, space charge effects could be eliminated by using single electron pulses[13,14] or relativistic electron energies.[15]

All these approaches use high energy electrons in the range of tens of keV in order to study bulk dynamics in a transmission geometry. Surface sensitivity is gained to some extent by using ~10 keV electrons in grazing incidence.[16–18] However, achieving sub-ps time resolution has been experimentally challenging.[19] Alternatively, using lower-energy electrons creates the potential for unprecedented insight into the dynamics at surfaces and nanostructures, but fs time resolution has yet to be implemented in methods such as low-energy electron diffraction (LEED).[46]

In diffraction, the achievable spatial resolution is given by the coherence of the source. For femtosecond electron guns based on flat photocathodes, the transverse coherence length at the sample position is usually limited to a few nanometers,[1] which constitutes one of the clear disadvantages of UED to date. In this regard, the idea of fs-photo cathodes based on nanometer-sized, quasi-point-like

a)Electronic mail: alexander.paarmann@fhi-berlin.mpg.de.
b)Electronic mail: sschaefer@ump.gwdg.de.

 

photoemitters[20,21] which exhibit intrinsically large transverse coherence[22] is very appealing, especially in combination with single-electron operation.

Recently, much effort was put into investigating the microscopic mechanisms of electron emission from metallic nanotips triggered by femtosecond laser pulses.[20,21,23–30] Depending on the tip's size, shape, and material, applied dc voltage, and laser intensity, various regimes of laser-tip interaction and photoemission were observed. With increasing laser intensity, the regimes of laser-induced electron emission are commonly discussed as photo-assisted field emission,[24–26] multiphoton photoemission,[21,23] above threshold photoemission,[27,28] and optical field emission.[29–31] These regimes are often characterized by the Keldysh parameter $\gamma$.[32] In these experiments, measuring the energy spectra and spatial emission patterns of the photoemitted electrons provided the basis of the discussion. Here, the width of the energy spectra is found to steadily increase from several 100 meV to many eV (Refs. 21, 26, 27, and 31) with increasing optical nonlinearity of the emission process, with the corresponding laser peak intensities on the tip apex in the range of $\sim 10^9 - 10^{12}$ W/cm$^2$. The spatial emission patterns can reflect the local work function for photo-assisted field emission,[25] but is otherwise structureless, and emission generally occurs into solid angles in the range of 0.15-0.3 sr.[21,25,30]

The dynamics of the photoemission and the resulting electron pulse duration was discussed in some detail for the various emission regimes.[23,26,28,31,33] The nonlinearity of the photoemission process generally leads to electron pulses shorter than the intensity profile of the exciting laser pulse. However, the effective electron pulse duration is ultimately determined not only by the generation process, but also by the propagation from the source to a sample.[1] Pulse broadening during propagation was extensively studied for high-kinetic-energy, many-electron pulses from flat cathodes, including the electron optics and space charge broadening.[10,34,35] The situation is quite different when using nanotips as ultrafast electron sources, where only moderate acceleration voltages can be applied and the nanoscopic geometry of the emission site can heavily influence the electron pulse characteristics. The lower bias voltages typically applied to nanotips intrinsically support their usage as low-energy fs electron sources.

Here, we investigate the propagation of single-electron pulses photoemitted from metal nanotips in two different geometries. First, we employ the simplest possible geometry, consisting of a negatively biased nanotip placed above a flat anode, see Fig. 1(a). This anode can represent an ultrathin sample or a nanoscopic object to perform time-resolved electron imaging or electron holography,[36] making use of the diverging electron beam generated at the nanotip. Second, collimated or focused fs electron beams can be generated in the second geometry we study here, which resembles the design of commercial static field-emission guns[37] used in transmission electron microscopes (TEM), see Fig. 1(b). In our simulations, we parameterize the photoelectron distributions with regard to their initial energy and spatial distribution as a means to describe the various regimes of nonlinear photoemission. This approach makes our results applicable to a wide range of experimental irradiation conditions. Our design study identifies the critical parameters to achieve sub-ps time resolution in pump-probe experiments for a nanotip-based low-energy electron gun.

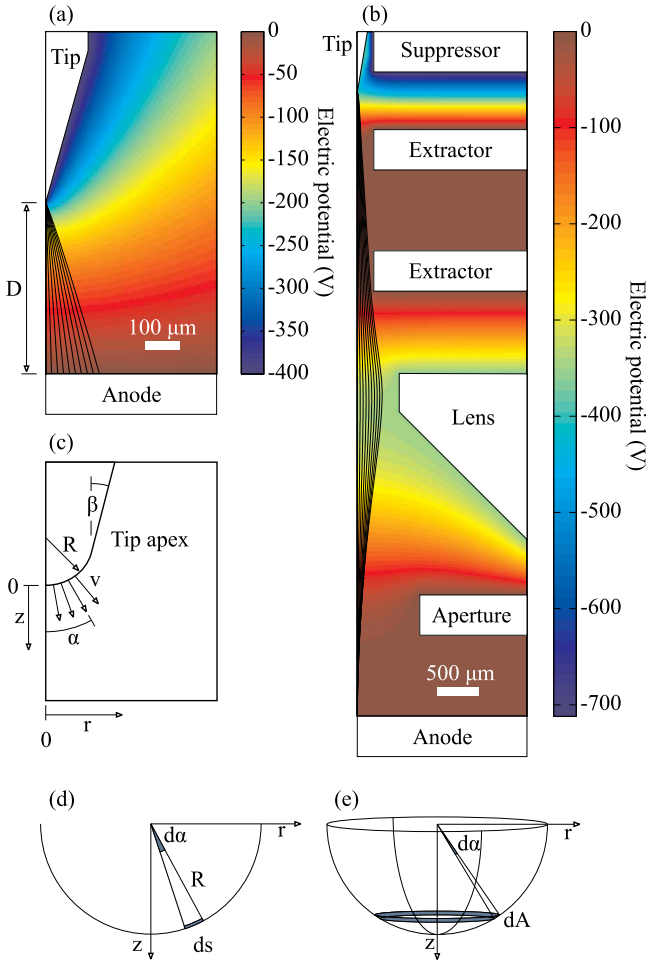


FIG. 1. Simulation geometry and electrostatics. Electric potentials (contour surfaces) and example electron trajectories (black lines) are shown for the tip-anode geometry (a) and TEM-optics geometry (b) for $U_{tip} = -400$ V and $R = 25$ nm. For (a), $D = 500$ $\mu$m, for (b) $D = 7.7$ mm, $U_{sup} = -712$ V and $U_{lens} = -345$ V. Please note the different scales in (a) and (b). (c) Illustration of the parameters $\alpha$ and $v$ for the electron trajectory simulations, the $(r, z)$-coordinate system, the tip opening angle $\beta$, and the tip radius $R$. (d) and (e) Illustration of the coordinate transformation between emission angle and emission area in 2D and 3D, respectively.

## II. SIMULATION PROCEDURE

For both geometries considered here, the tip-anode geometry and the TEM-optics geometry, see Figs. 1(a) and 1(b), respectively, the potential equation $\Delta U = 0$ is solved by a finite element method (FEM), where $U$ is the electrostatic potential. Cylindrical symmetry was assumed in all simulations, which significantly reduces the computational cost. Details are described in the Appendix. Cylindrical coordinates $x = \{r, z\}$ are used throughout the paper. The electric potentials obtained from such calculations are shown in Figs. 1(a) and 1(b). The maximum electric fields at the tip reach values of up to 10 GV/m, correctly reproducing the geometrical dc field enhancement.[38] In the TEM-optics geometry, this dc field enhancement can be largely suppressed, depending on the specific biases applied.

The geometry of the emission tip is adapted from the typical shape of nanotips produced from electro-chemically etched metal wires.[20,21,25] Specifically, we assume the needle emitter to have a conical tip with a half opening angle $\beta$ taken as 15.5°, and a spherical apex with radius $R$ in the range of $R = 10$–$100$ nm. The shaft of the tip is modelled as cylinder with a radius of 125 $\mu$m, see Fig. 1. We apply a negative bias $U_{tip}$ to the tip, the flat anode is kept at ground potential. In the tip-anode geometry, the position of the anode is varied, at a distance $D$ from the tip. In the TEM-optics geometry, the anode is kept fixed at $D = 7.7$ mm. The lens assembly consists of a suppressor unit (negative bias voltage $U_{sup}$ with respect to tip), an extractor (positive bias voltage $U_{ex}$ with respect to tip), an electrostatic lens (variable bias voltage $U_{lens}$, depending on focus), and an aperture kept at ground potential, see Fig. 1(b).

Electron wave packet propagation is simulated classically by solving the equation of motion within the MATLAB programming environment for single electrons in the computed electric field $\nabla U$ using a Runge-Kutta algorithm. Particular attention was paid to high-precision interpolation of the fields in proximity of the tip apex. We assume $\leq 1$ electron per pulse, so that space charge effects can be neglected, consistent with experiments using high repetition rate, low pulse energy laser sources.[21,25,27]

Electrons photoemitted from metal nanotips exhibit distinct spatial (emission site area and angular spread) and temporal properties depending on the various experimental parameters, e.g., laser intensity, center wavelength, and pulse duration, tip radius, dc voltage, as well as crystal structure and orientation.[25,27,30] For generality, we describe the initial laser-excited electron wave packets by a Gaussian distribution of the emission site on the tip apex, as well as a Gaussian distribution of the initial kinetic energy $E$ of the photoelectrons. In particular, we assume electron emission perpendicular to the tip surface with initial velocity $\vec{v} = \{|v|\sin(\alpha), |v|\cos(\alpha)\}$, where $|v| = \sqrt{\frac{2}{m_e}E}$ and $\alpha$ the emission angle with respect to the symmetry axis,[39] see Fig. 1(c). Then, the angular momentum vanishes and the equations of motions are simply $\ddot{X} = (e/m_e)(\partial_r U(X), \partial_z U(X))$. In that case, Gaussian distributions of the emission site on the tip surface are conveniently reproduced by Gaussian distributions of the emission angle $\alpha$, since $d\alpha = R \cdot ds$, where $ds$ is the differential line element on the tip curvature, see Fig. 1(d). Then, the initial electron wave packet can be described by

$$F(E,\alpha) = F_0 \cdot \theta(E)\exp\left[-\frac{(E-E_0)^2}{2\sigma_E^2} - \frac{\alpha^2}{2\sigma_\alpha^2}\right], \qquad (1)$$

where $\theta(E)$ is the Heaviside function and proper normalization is ensured by the factor $F_0$. Along the kinetic energy direction, the distributions are cut off at $E = 0$.

These assumptions provide a good approximation of the electron energy spectra observed in several experiments investigating the different regimes of (nonlinear) photoemission from nanotips.[21,26,27] We note that more complex electron spectra, e.g., those shown in Ref. 26, can easily be analyzed by modifying the energy component of Eq. (1) accordingly.

The properties of the electron wave packet during propagation and at the anode are analyzed by evaluating the single electron trajectories $X(E,\alpha,t) = \{X_r(E,\alpha,t), X_z(E,\alpha,t)\}$, $t$ being the propagation time, weighted by their statistical probability according to $F(E,\alpha)$. Specifically, we analyze the spatio-temporal distributions $S(x,t)$

$$S(x,t) = \iint dE d\alpha\, \delta(x - X(E,\alpha,t))F(E,\alpha). \qquad (2)$$

For illustration, in the tip-anode geometry, we compare $S$ in Fig. 2, for $\sigma_E = 0.5$ eV and 3.0 eV with $E_0 = 0.5$ eV, $\sigma_\alpha = 10°, D = 100\,\mu$m, $U_{tip} = -200$ V, and $R = 50$ nm for multiple propagation times $t = 1$–$12$ ps, where the effects of beam divergence and velocity dispersion are clearly visible.

We then analyze the spot size at the position of the anode as indicated in Fig. 1. The electron spot at the anode is defined as the radial distribution $\rho(r)$ of the electron wave packet

$$\rho(r) = \iint dE d\alpha\, \delta(r - \Delta(E,\alpha))F(E,\alpha), \qquad (3)$$

with $\Delta$ the radial arrival position at the anode

$$\Delta(E,\alpha) = \int dt\, \delta(X_z(E,\alpha,t) - D)X_r(E,\alpha,t). \qquad (4)$$

The standard deviation $\sigma_\rho$ of $\rho(r)$ with respect to the beam center $r = 0$, i.e., $\sigma_\rho = \sqrt{\langle \rho(r)^2 \rangle}$, gives a good measure of the electron spot size at the anode position and can also be used to estimate the divergence of the electron beam. In

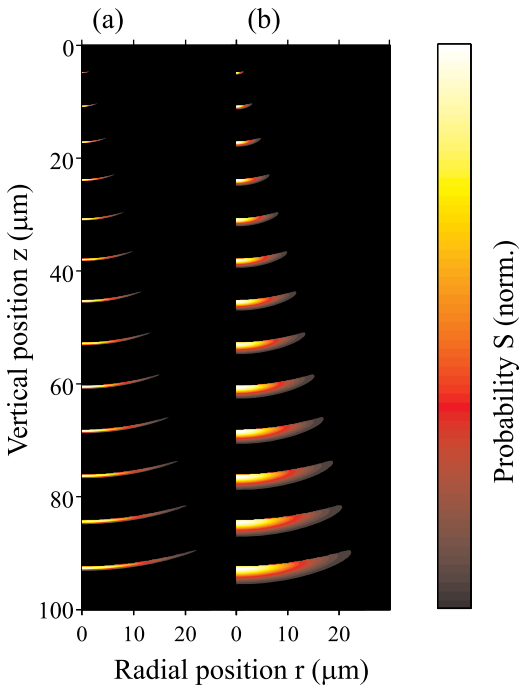


FIG. 2. Tip-anode geometry: time series of spatial electron distributions $S(x,t)$ in steps of $\Delta t = 1$ ps for $E_0 = 0.5$ eV, $\sigma_\alpha = 10°$, $D = 100\,\mu$m, $U_{tip} = -200$ V, and $R = 25$ nm. We compare two different energy distributions with $\sigma_E = 0.5$ eV (a) and $\sigma_E = 3.0$ eV (b). Each distribution was normalized for its respective maximum.

Figs. 3(a) and 3(b), we show selected distributions $\rho(r)$ for a range of $\sigma_\alpha$ and $\sigma_E$, respectively. Clearly, the energy spread $\sigma_E$ has no detectable effect on $\rho(r)$, whereas the width of the distribution linearly follows $\sigma_\alpha$, since $\tan(\alpha) \sim \alpha$ in this range.

We also evaluate the time-of-flight distribution $\tau(t)$, i.e., the probability of finding the electron at the anode vertical position $z = D$ at time $t$. Opposed to the above treatment to analyze spatial distributions in 2D, the time-of-flight distributions need to be corrected for the three dimensional emission site distribution on the tip surface. For that purpose, the distribution function, Eq. (1), needs to be modified to account for the emission area $dA = 2\pi R^2 \sin(\alpha) d\alpha$ on the half-spherical tip surface at emission angle $\alpha$, see Fig. 1(e),

$$G(E, \alpha) = G_0 \cdot \sin(\alpha) F(E, \alpha), \tag{5}$$

where the proper normalization of the distribution is ensured by $G_0$. Then, the time-of-flight distribution is given by

$$\tau(t) = \iint dE d\alpha \, \delta(t - \Theta(E, \alpha)) G(E, \alpha), \tag{6}$$

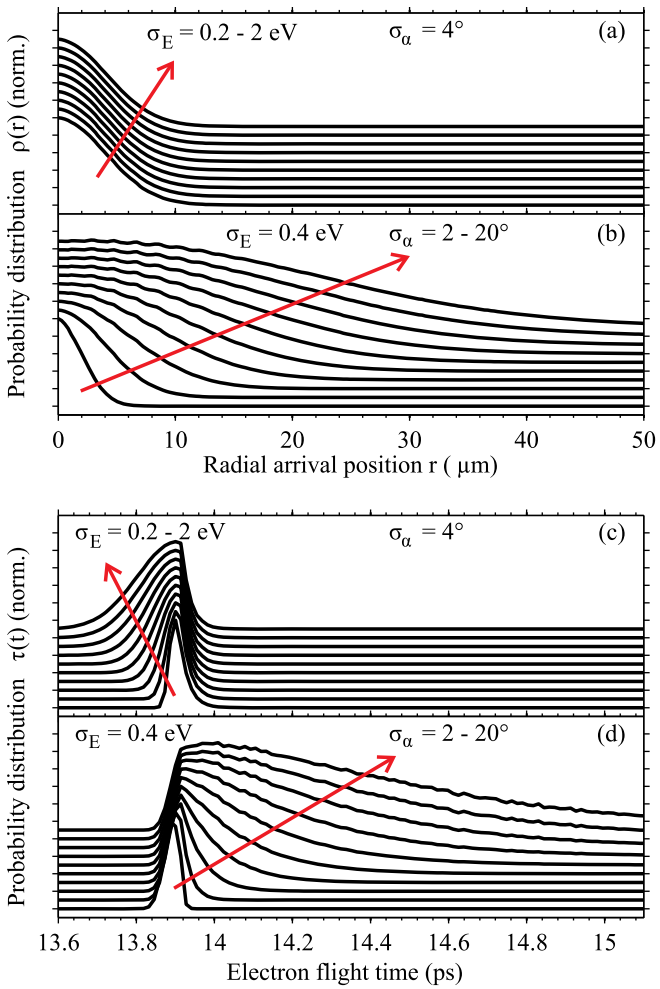


FIG. 3. Tip-anode geometry: radial distributions $\rho(r)$ ((a), (b)) and time-of-flight distributions $\tau(t)$ ((c), (d)), shown for a range of $\sigma_E$ at $\sigma_\alpha = 4°$ ((a), (c)) and for a range of $\sigma_\alpha$ at $\sigma_E = 0.4$ eV ((b), (d)). The remaining parameters are identical to Fig. 2. The plots were offset vertically for clarity and each plot is normalized for its maximum.

where the time of flight $\Theta(E, \alpha)$ of an individual trajectory is given by

$$\Theta(E, \alpha) = \int dt \delta(X_z(E, \alpha, t) - D) t. \tag{7}$$

The standard deviation of the time-of-flight distributions $\sigma_\tau = \sqrt{\langle (\tau(t) - \langle \tau(t) \rangle)^2 \rangle}$ as a function of $\sigma_E$ and $\sigma_\alpha$ is related to the effective full-width-at-half-maximum (FWHM) electron pulse duration at the anode.[40] Figs. 3(c) and 3(d) show a few selected distributions of $\tau(t)$ for a range of $\sigma_\alpha$ and $\sigma_E$, respectively. It is immediately obvious that the shape of $\tau(t)$ can be highly asymmetric depending on the specific combination of $\sigma_E$ and $\sigma_\alpha$.

Statistical analysis was performed by projecting rectangular phase space areas out of an evenly spaced grid of the initial parameters $(E, \alpha)$ onto the target phase space, i.e., spatial coordinates, time-of-flight, or radial position at the anode, respectively. The resulting target distributions are intrinsically smooth and converge quickly with regard to the $(E, \alpha)$ grid density, compared to point projection and histogram analysis.

Within the TEM-optics geometry, two subsystems are simulated in order to determine the optimal settings for the electrostatic lens assembly with respect to pulse duration and beam waist. First, the subsystem of suppressor, tip, and extractor is analyzed, with the extractor and all consecutive voltages set to a common potential. To find the optimal operating regime for the given subsystem, the suppressor voltage is scanned while keeping the extractor and tip voltages fixed. In the next step, the lens and aperture are taken into account. While operating suppressor, extractor and tip at the previously determined optimal settings, the lens voltage is scanned to find the region of smallest beam waist, while maintaining high temporal resolution. The final aperture is always kept at ground potential, therefore, the electron kinetic energy at the exit of the assembly depends only on the tip potential.

The effect of the duration of the electron emission process can be modelled on many levels of theory.[26,29,30,41,42] For a multiphoton excitation with laser pulses short compared with electronic relaxation times within the metal tip,[21] the temporal profile of the electron emission process follows the $n$th power of the laser intensity envelope, $n$ being the dominant order of the multiphoton emission process. For longer optical pulse durations, more sophisticated models including the electron population build up and relaxation were reported.[26] On the opposite end, extremely short emission times are expected for higher optical field strength, i.e., above threshold photoemission and optical field emission.[28–30,42] For experimental laser pulse durations of 5–30 fs typically used in the nonlinear photoemission regimes,[20,21,27,30] the pulse broadening during the electron propagation will be much larger than the duration of the electron emission process for most cases, thereby dominating the experimentally relevant electron pulse duration. In the following, we therefore assume a prompt electron emission. When using longer optical pulses, e.g., on the order of 100

fs,[25,26] a finite duration of the emission can be included by convolving the time-of-flight distribution $\tau(t)$ with the respective electron emission temporal profile.

## III. RESULTS

### A. Tip-anode geometry

The main temporal and spatial characteristics of electron pulses emitted from metal nanotips are qualitatively well captured in Fig. 2. The electrons experience an extremely inhomogeneous field: the majority of the acceleration occurs in close proximity of the tip, i.e., within the first $\lesssim$100 nm. For initial kinetic energies small compared with the acceleration voltage, i.e., $E_{kin} \ll e|U_{tip}|$, the electrons closely follow the dc field lines in this region. The remainder of the propagation is almost field-free, and the electron wave packet simply evolves according to the forces experienced close to the tip. In consequence, the spatio-temporal distributions $S(x, t)$ are strongly influenced by path length differences between on-axis and off-axis electron trajectories.

In most of the parameter range studied here, these path length differences dominate the electron pulse duration. This behavior is depicted in Fig. 4(a) where we plot $\sigma_\tau$ as a function of $\sigma_\alpha$ and $\sigma_E$, for $D = 100\,\mu$m, $R = 25$ nm, and $U_{tip} = -200$ V. In this contour plot, horizontal contour lines correspond to the regime where wave packet dispersion is the main pulse broadening mechanism, whereas vertical contour lines indicate pulse broadening due to path length differences, i.e., beam divergence. This is further illustrated by the horizontal and vertical line profiles shown in Figs. 4(b) and 4(c). Only for small angular spread $\sigma_\alpha \lesssim 6^\circ$, corresponding to emission into 0.05 sr, we observe a significant dispersive pulse broadening. For larger angular spread, the pulse duration is essentially insensitive to $\sigma_E$, even up to very large values of $\sigma_E = 2$ eV. The transition between dispersive and path length pulse broadening is well captured in the convergence between the two curves in Fig. 4(b).

The absolute numbers of $\sigma_\tau$ seen in Fig. 4 range from <50 fs to >450 fs. The increasing asymmetry of the distribution $\tau(t)$ with increasing $\sigma_\alpha$, see Fig. 3, causes the FWHM of $\tau(t)$ to not increase as steeply as $\sigma_\tau$. In fact, for large angular spreads $\sigma_\alpha \gtrsim 10^\circ$ the FWHM is comparable to $\sigma_\tau$, indicative of an extremely asymmetric pulse form with a very long tail. It is possible that some experimental approaches can make specific use of such pulse shapes with steeply rising and slowly decaying edges. However, for most time-resolved studies, the standard deviation $\sigma_\tau$ will be the most useful quantity in determining the effective electron pulse duration.

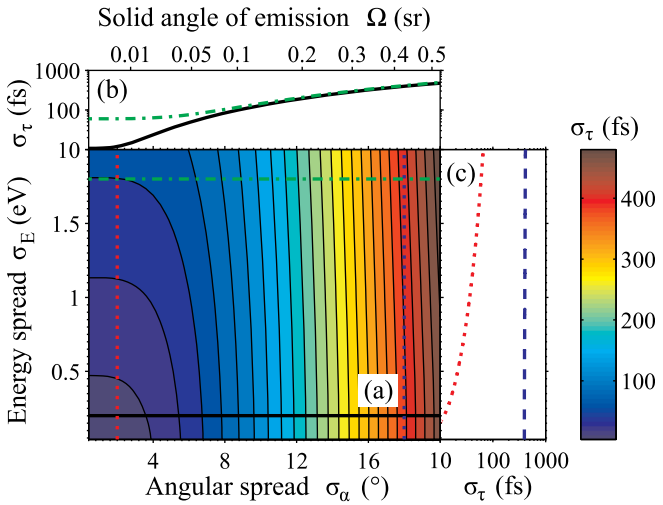


FIG. 4. Pulse duration in the tip-anode geometry. (a) Contour plot of $\sigma_\tau$ as a function of $\sigma_\alpha$ and $\sigma_E$. Contour lines are drawn every 25 fs. The horizontal and vertical lines indicate the positions of the line profiles shown in (b) and (c), respectively, taken at $\sigma_E = 0.2$ eV (black, solid line), $\sigma_E = 1.8$ eV (green, dashed-dotted line), $\sigma_\alpha = 2^\circ$ (red, dotted line), and $\sigma_\alpha = 18^\circ$ (blue, dashed line). Simulation parameters: $D = 100\,\mu$m, R = 25 nm, $U_{tip} = -200$ V. The top axis shows the corresponding solid angle of emission $\Omega = 2\pi(1 - \cos(\sqrt{(2\log(2))}\sigma_\alpha))$.

Fig. 5(a) shows a contour plot of $\sigma_\tau$ as a function of the tip voltage $U_{tip}$ and the initial angular spread $\sigma_\alpha$, for $D = 100\,\mu$m, $R = 25$ nm. The initial kinetic energy spread is kept fixed at $\sigma_E = 0.5$ eV, in good agreement with a multiphoton excitation process.[21,25] As expected, the electron pulses generally get shorter with higher tip voltage. However, we again observe a transition of the behavior at

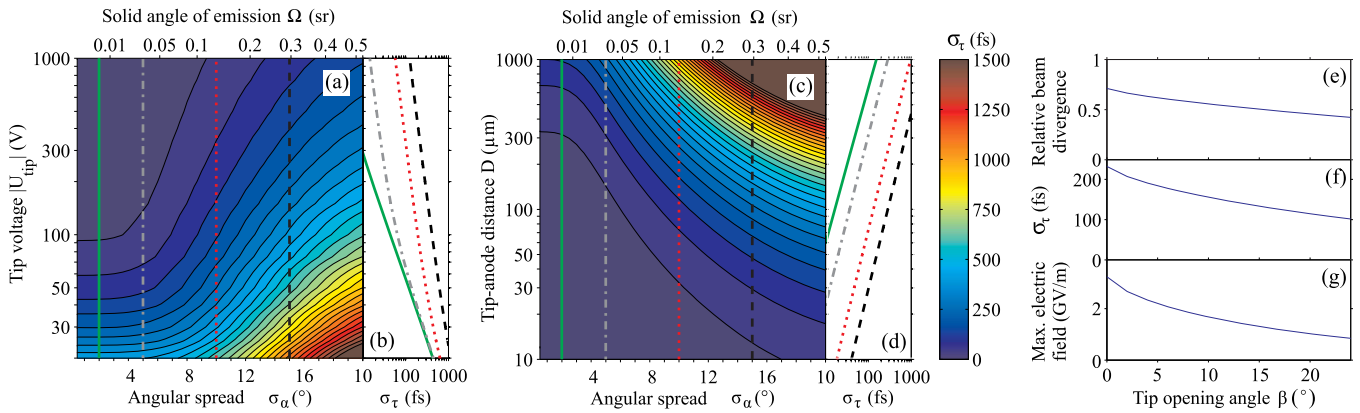


FIG. 5. Tip-anode geometry: (a) and (c) show contour plots of the pulse duration $\sigma_\tau$ as a function of the angular spread $\sigma_\alpha$ for varied tip voltage $|U_{tip}|$ (a) and tip-anode distance $D$ (c). Contour lines are drawn every 50 fs. Vertical lines indicate the positions of line profiles depicted in (b,d) taken at $\sigma_\alpha = 2^\circ$ (green, solid line), 5° (gray, dotted-dashed line), 10° (red, dotted line), and 15° (black, dashed line). Please note the logarithmic scales. Plots (e)-(g) illustrate the effect of the tip opening angle $\beta$: the relative reduction of the beam divergence after propagation (e) as compared to the initial distribution also causes the reduction of the pulse duration (f), despite the reduced field enhancement at the apex (g). Simulation parameters: $R = 25$ nm, $\sigma_E = 0.5$ eV, $D = 100\,\mu$m ((a), (b), (e)-(g)), $U_{tip} = -200$ V ((c)-(g)) and $\sigma_\alpha = 10^\circ$ ((e)-(g)).

$\sigma_\alpha \sim 5°$: above this value, the electron pulse duration scales as $\sigma_\tau \propto 1/\sqrt{|U_{tip}|}$, as indicated by the linear behavior in the doubly logarithmic plot in Fig. 5(b). Only at smaller $\sigma_\alpha$, dispersive pulse broadening can contribute to the voltage dependence, see the green, solid line in Fig. 5(b).

The dependence of $\sigma_\tau$ on the tip-anode distance $D$ is shown in Figs. 5(c) and 5(d), calculated for $R = 25$ nm, $U_{tip} = -200$ V, and $\sigma_E = 0.5$ eV. For all $\sigma_\alpha$, we observe a slightly sub-linear behavior, i.e., $\sigma_\tau \propto D^\gamma, \gamma \sim 0.95$. Very similar sub-linear behavior is also observed for the spot size $\sigma_\rho$ and is likely caused by the reduced field enhancement and, in consequence, reduced inhomogeneity in the electron acceleration with increasing $D$.

We find the tip radius $R$ to have little impact on the overall electron propagation. When increasing the tip radius from $R = 10$ to 100 nm, $\sigma_\tau$ and $\sigma_\rho$ both increase by $\sim$10 %. This is another manifestation of the effect causing the sublinear behavior observed on changing the tip-anode distance $D$ in Fig. 5. When increasing $R$ while maintaining all other parameters, the reduced field enhancement also reduces the total inhomogeneity of the electron acceleration.

The spot size at the anode position is essentially independent of the tip voltage, the tip radius $R$ and the electron energy spread $\sigma_E$, while it scales linearly with the angular spread $\sigma_\alpha$ and the tip-anode distance $D$. However, the conical shape of the tip and the resulting field lines deform the electron trajectories, leading to an overall reduction of the beam divergence compared to the initial distribution, i.e., $\sqrt{\langle \arctan(v_r(\Theta)/v_z(\Theta))^2 \rangle}/\sigma_\alpha^2$. As can be seen in Fig. 5(e), this effect scales strongly with the opening angle of the tip apex, and is in the range of 0.7 and 0.4 for $\beta = 0 - 24°$. In the regime of path length pulse broadening, this geometric effect also results in significant reduction in the pulse duration, see Fig. 5(f), even though the reduced effective sharpness of the needle also significantly reduces the dc field enhancement (g). Essentially, increasing $\beta$ flattens the photo cathode and reduces the divergence and path length differences in the electron beam.

### B. TEM-optics geometry

We now turn to the analysis of the temporal and spatial characteristics of a short electron pulse in the more complex TEM-optics geometry, which comprises a suppressor-extractor assembly with an electrostatic lens, see Fig. 1(b). To determine the optimal settings for the electrostatic lens assembly with respect to pulse duration and beam waist, we first perform simulations within the subsystem of suppressor, tip, and extractor and take the influence of the lens into account in the second part of this subsection. For all results shown in this subsection, we assume $\sigma_\alpha = 10°$.

First, the qualitative effect of a suppressor-extractor geometry (without electrostatic lens) is analyzed. Electrons are initially radially accelerated away from the tip, resulting in a strongly diverging beam, as discussed above. However, within the plate-capacitor-like field distribution between suppressor and extractor electrode, the beam divergence can be reduced by accelerating the electrons in the direction along the electron optical axis. Depending on the tip potential relative to the plate capacitor potential (generated by suppressor and extractor) in the region of the tip apex, three situations can be considered and compared to the tip-anode geometry. A tip potential much lower than the plate capacitor potential would lead to strongly divergent trajectories in the vicinity of the tip, very similar to the tip-anode

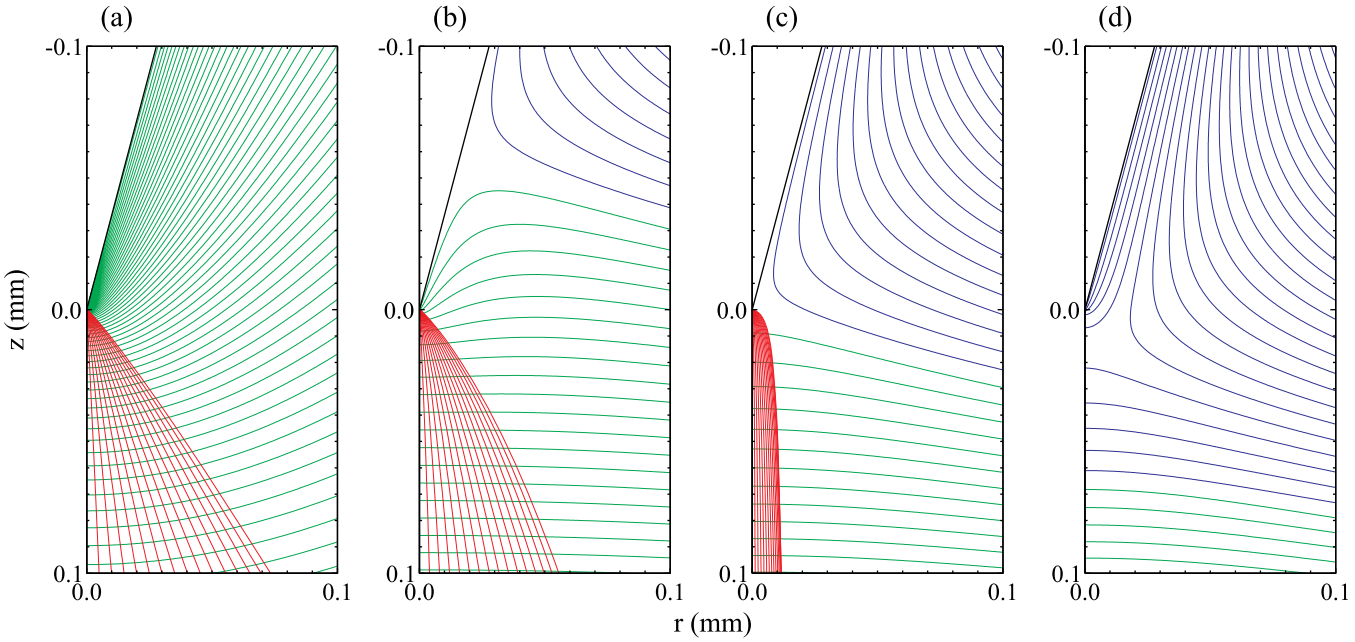


FIG. 6. Suppression of the field enhancement in the TEM-optics geometry. Equipotential contour lines in steps of 5 V are shown in the vicinity of the emission tip, (a) for the tip-anode geometry, and for the suppressor-extractor geometry (b)-(d) for different suppressor potentials of $U_{sup} = -634$ V (b), $U_{sup} = -734$ V (c), and $U_{sup} = -834$ V (cutoff voltage, (d)) with the extractor kept at ground potential and the tip held at $-400$ V. Contours are drawn in blue for $U < -400$ V and in green for $U > -400$ V to visualize the relative potentials of the tip and effective plate capacitor created by the suppressor-extractor assembly. The red lines represent electron trajectories with $E = 0.5$ eV at various emission angles. No electron emission occurs for $U_{sup} = -834$ V (cutoff voltage, (d)) due to the field reversal at the apex surface.

geometry, see Figs. 6(a) and 6(b), and therefore to large discrepancies in the length of the trajectories for electrons from different emission sites as discussed in Subsection III A.

When reducing the difference between the apex and the surrounding plate capacitor potential, the electron trajectories become radially squeezed, Fig. 6(c), until the tip voltage is above the plate capacitor potential and electron emission is suppressed at the cutoff voltage, Fig 6(d), since the electric field direction at the apex surface is now reversed. By squeezing the electron trajectories, the path length differences between on-axis and off-axis electron trajectories are reduced, leading to an improved temporal width of electron pulses. However, at the same time, the field enhancement around the tip apex is increasingly suppressed, reducing the electron acceleration within the vicinity of the tip so that a more pronounced dispersive electron pulse broadening, compared with the tip-anode geometry, is expected. Balancing these two effects by tuning the suppressor voltage for a given initial kinetic energy distribution should lead to an optimal temporal pulse width. To find the optimal suppressor operating regime for the given geometry, the tip voltage is set to −400 V, the extractor and all subsequent voltages are held at ground potential and the suppressor voltage is scanned between −735 V and −600 V.

Fig. 7 shows the pulse duration dependence on the suppressor voltage at different initial electronic energy distributions widths $\sigma_E$. For $\sigma_E = 0$ eV, the pulse duration continuously decreases as the suppressor voltage approaches the cutoff voltage. At the cutoff voltage, off-axis trajectories are suppressed and path length differences no longer contribute to the temporal pulse broadening. At finite $\sigma_E$, the curves exhibit a steep increase in pulse duration close to the suppressor cutoff voltage, since at this point the field enhancement at the tip is no longer operative. Then, the width of the initial electronic energy distributions $\sigma_E$ gives a large contribution to the dispersive temporal broadening.

An optimal balance between increased dispersive pulse broadening and decreased path length-induced broadening is realized at an intermediate suppressor potential. For $\sigma_E = 0.2$ eV, the optimal suppressor voltage is −712 V, resulting in electron pulses with a temporal width of about 0.5 ps. With increasing $\sigma_E$, the optimal suppressor voltage setting shifts to higher suppressor potentials because the suppression of dispersive pulse broadening becomes more important. Hence, a stronger acceleration close to the tip becomes beneficial in this case.

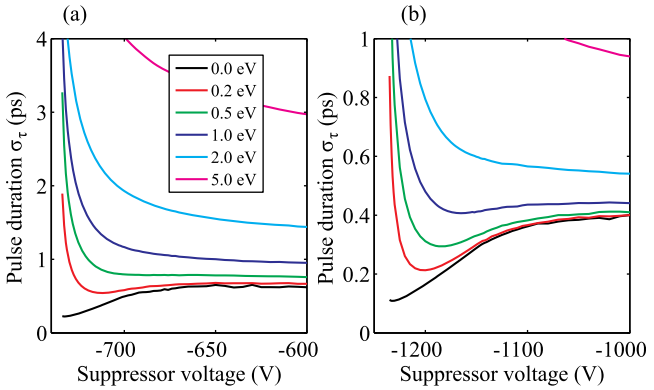


FIG. 7. Suppressor-extractor geometry. Pulse durations $\sigma_\tau$ at the anode for various energy widths $\sigma_E$ are plotted for extractor voltage $U_{ex} = 0$ V (a) and $U_{ex} = +600$ V (b). Please note the different scales in (a) and (b).

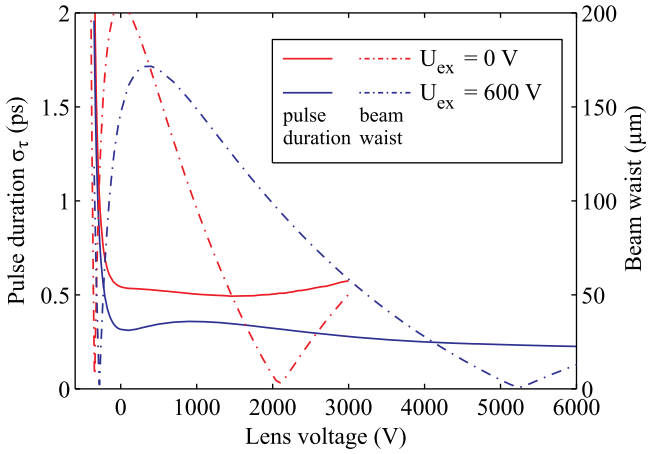


FIG. 8. Pulse durations and beam waist in the TEM-optics geometry. The temporal pulse width $\sigma_\tau$ (solid curves, left axis) and beam waist (dotted-dashed curves, right axis) at the anode are plotted as a function of the lens potential. Two extractor voltage settings are shown: $U_{ex} = 0$ V (red curves) and $U_{ex} = 600$ V (blue curves).

In order to further reduce the temporal pulse width, the suppressor-extractor field can be increased by applying a positive potential to the extractor. The resulting pulse durations are plotted in Fig. 7(b) for $U_{ex} = +600$ V at various values of $\sigma_E$. With this setting, sub-250 fs electron pulses can be generated at $\sigma_E = 0.2$ eV for the optimal suppressor voltage of $U_{sup} = -1200$ V.

Using the optimal suppressor settings for $\sigma_E = 0.2$ eV, we now take the influence of the full lens assembly into account, adding lens and aperture. The lens voltage $U_{lens}$ is scanned between −400 V and 6000 V, while the aperture is kept at ground potential and the extractor is either at ground potential or at +600 V, see Fig. 8.[43] The electrostatic lens element can be used both in an accelerating mode ($U_{lens} > U_{ex}$) and an decelerating mode ($U_{lens} < U_{ex}$), both leading to a focusing effect on the electron beam, i.e., the beam waist depending on the lens voltage exhibits two minima, see Fig. 8. One focus occurs close to the tip voltage (decelerating regime) at $U_{lens} = -345$ V for $U_{ex} = 0$ V and at $U_{lens} = -280$ V for $U_{ex} = 600$ V, with beam waists of ∼6 μm and ∼2 μm, respectively. The second focus (accelerating regime) occurs at 2100 V and 5250 V for the two extractor settings, where the beam waists are even reduced by a factor of 3. In the decelerating regime, the pulse duration increases very steeply when reducing $U_{lens}$ because here electrons travel at low kinetic energies in the lens region. In this case, the finite energy dispersion leads to a strong temporal broadening. In the accelerating regime, the electron traveling time is strongly reduced, resulting in much shorter pulse durations of ∼0.5 ps and ∼0.23 ps for $U_{ex} = 0$ V and $U_{ex} = +600$ V, respectively.[44]

## IV. DISCUSSION

The two geometries studied here offer two alternative approaches to time-resolved experiments employing short low-energy electron pulses. The tip-anode geometry is more

flexible and allows for very short propagation distances simply by using a very compact setup. With the diverging electron beam, it is well-suited for time-resolved electron imaging applications. The TEM-optics geometry offers full beam collimation control, making it suitable for electron diffraction studies, where focusing of the beam onto a detector or a sample is desired.

In the tip-anode geometry, pulse temporal broadening is dominated by path length differences within the diverging beam for typical experimental parameters. Short tip-anode distances and large tip biases produce the shortest electron pulses. While we find negligible influence of the tip radius on the electron propagation, the opening angle of the tip apex has a significant effect on the pulse duration and divergence of the electron beam. These findings combined with the parameter ranges for the different photoemission regimes discussed in the introduction allow for several experimental scenarios to produce short electron pulses at variable electron energies.

If short-pulse low-divergence beams at low electron energies are desired, the usage of nanotips with rather large opening angle and apex radius is optimal in combination with short tip-anode distance operation. Such tip geometry minimizes the dc field emission, allowing for good contrast of the photo current. However, such a geometry also reduces the optical field enhancement, and very short optical pulses at relatively high pulse energies and low repetition rate to avoid thermal damage to the nanotip are likely the best approach. Even then, a minimum of optical field enhancement must be maintained in order to restrict the photoemission to the apex and suppress emission from the much larger tip shaft area. If high divergence beams are needed for imaging applications, an apex with low opening angle is much better suited. The shortest electron pulses are obtained with higher bias and consequently higher electron energies.

Some control of the emission area for photo-assisted field emission was achieved by manipulating the laser polarization as well as the tip polar and azimuthal orientation.[25] We expect a similar type of control is likely possible for multiphoton photoemission using the dc bias to change the local work function through the Schottky effect,[26] thereby manipulating the effective local multiphoton order.

Alternatively, when employing the TEM-optics geometry, we predict full control over the electron beam collimation while at the same time the path length differences are minimized, and velocity dispersion is dominating the temporal broadening of the electron pulse. Additionally, the electron optics design considered here offers the possibility to optimize the electron pulse duration for a given energy spread by a proper setting of suppressor and extractor voltages. In particular, tuning of the suppressor-extractor field allows to modify the dc field enhancement at the apex and therefore decouples the tip bias from the emission mechanism, so that higher biases can be utilized while suppressing the dc field emission. At the same time, the suppressor-extractor field can remove most of the path-length differences in the electron wave-packet, recovering the dispersive broadening as the limiting factor for the pulse duration. As an example for a moderate tip bias of 400 V and narrow-band electron pulses ($\sigma_E = 0.2$ eV), we find pulse durations of 230 fs despite a rather long propagation length of 7.7 mm in our design. Using an electrostatic lens to focus the electron pulse onto the sample does not lead to a deterioration of the temporal pulse width.

With velocity dispersion as the dominant broadening mechanism, in particular for broader electron spectra, it is clear that the size of the electron optics remains the main challenge to reach even shorter pulse durations. If electron optics were to be combined with rf-compression techniques established for high-energy electron pulses[11] to compensate for this problem, one still has to keep in mind the spatial wave packet distortion as depicted in Fig. 2, likely making it challenging to compress such non-Gaussian distributions. More compact designs of electron collimation optics are an alternative strategy to reduce the effect of the dispersive pulse broadening while eliminating the path length differences.

## V. CONCLUSIONS

The suitability of photo-excited nanotips as coherent femtosecond low-energy electron sources for time-resolved optical pump-electron probe experiments is investigated numerically. The propagation of the electron pulse from the nanotip to a sample is simulated in a simple tip-anode geometry and a suppressor-extractor geometry with electrostatic focusing lens. Classical electron trajectories in the highly inhomogeneous field are calculated and analyzed statistically to provide spatio-temporal properties of the electron pulses during propagation and at a sample.

The tip-anode geometry is found to be well-suited for time-resolved electron imaging applications, making use of the diverging electron beam. Path length differences within this divergent beam are the dominant cause of temporal pulse broadening, exceeding velocity dispersive broadening for typical experimental parameters. Using a very compact design, electron pulses as short as a few tens of femtoseconds are achievable.

With the TEM-optics geometry, it is possible to eliminate the majority of the path length broadening so that velocity dispersion is the main temporal broadening mechanism. This geometry gives full control over the electron beam collimation and some control over the pulse duration, which is ultimately limited by the 7.7 mm total propagation in our design. Still, we predict pulse durations as short as 230 fs in a focused beam. To further reduce the pulse durations, we suggest implementations of more compact electron optics to be the best approach for realizing a most versatile low-energy femtosecond electron gun based on metal nanotips.

## ACKNOWLEDGMENTS

We acknowledge helpful discussions with P. Hommelhoff. C.X. was partially funded by the Chinese Academy of Sciences. The authors from the University of Göttingen gratefully acknowledge financial support by the Deutsche Forschungsgemeinschaft (DFG-ZUK 45/1, SPP 1391, SFB 755).

## APPENDIX: NUMERICAL COMPUTATION OF THE ELECTROSTATIC POTENTIAL

We assume that $U = U(r, z)$ does not depend on the angular variable $\varphi$ in cylindrical coordinates $(r, \varphi, z)$ and that the geometry is rotationally invariant with respect to the $z$-axis with cross section $\Omega \subset \{(r,z) \in \mathbb{R}^2 : r \geq 0\}$. Then $U$ satisfies the boundary value problem

$$-\frac{1}{r}\frac{\partial}{\partial r}\left(r\frac{\partial U}{\partial r}\right) - \frac{\partial^2 U}{\partial z^2} = 0 \text{ in } \Omega \tag{A1a}$$

$$\frac{\partial U}{\partial \mathbf{n}} = 0 \text{ on } \Gamma_N \tag{A1b}$$

$$U = g_D \text{ on } \Gamma_D . \tag{A1c}$$

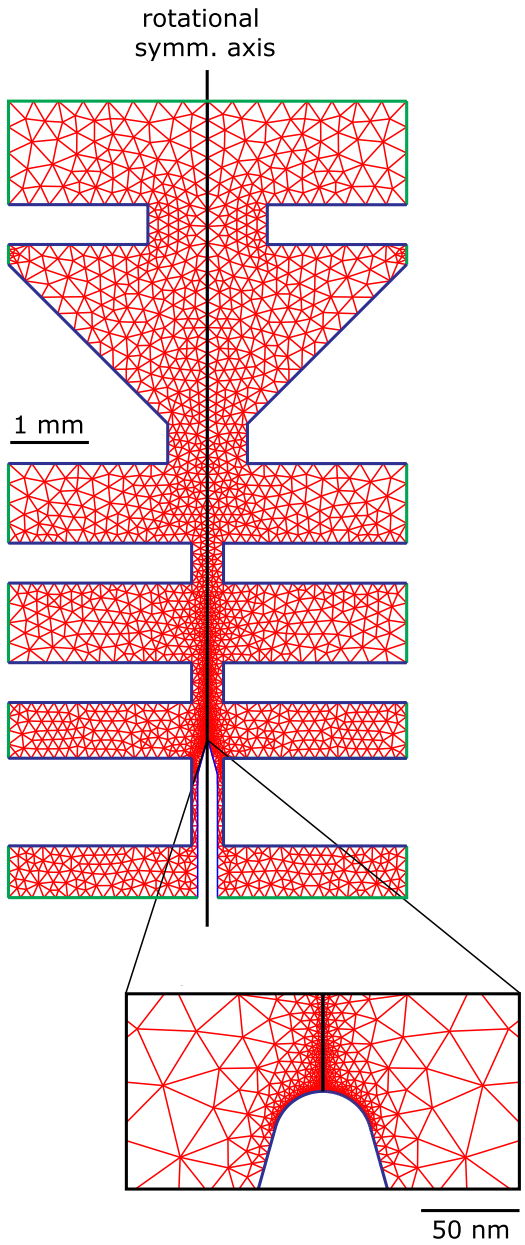


FIG. 9. FEM mesh. The FEM mesh utilized for TEM-optical geometry is shown before mesh refinement. At the boundaries either Neumann (green) or Dirichlet (blue) boundary conditions are adapted.

Here the boundary $\partial\Omega = \Gamma_D \cup \Gamma_N$ is divided into a part $\Gamma_D$ where Dirichlet boundary conditions are imposed and a part $\Gamma_N$ where homogeneous Neumann conditions are imposed (see Fig. 9). Multiplication of the differential equation (A1a) by a test function $V$ satisfying $V = 0$ on $\Gamma_D$, integration and partial integration yields

$$\int_\Omega \left(\frac{\partial U}{\partial r}\frac{\partial V}{\partial r} + \frac{\partial U}{\partial z}\frac{\partial V}{\partial z}\right) r d(r,z) = 0 . \tag{A2}$$

For a function $g$ on $\Gamma_D$ we introduce the set $\mathcal{V}_g$ of weakly differentiable functions $U$ on $\Omega$ satisfying $\int_\Omega (U^2 + (\frac{\partial U}{\partial r})^2 + (\frac{\partial U}{\partial z})^2) r\, d(r,z) < \infty$ and $U = g$ on $\partial\Omega_D$. Then the variational problem reads more precisely: Find $U \in \mathcal{V}_{g_D}$ such that Eq. (A2) holds true for all $V \in \mathcal{V}_0$. This problem was solved with the FEM (see, e.g., Ref. 45) using a geometry-adapted irregular FEM mesh shown in Fig. 9. The possibility to refine the mesh at the tip is particularly important for correctly evaluating the electric potentials and fields in the proximity of the nanoscopicly sharp tip as well as in transition into meso- and macroscopic scales. We employed both a self-developed high-order MATLAB finite element code and the commercial software package (COMSOL MULTIPHYSICS 4.2), and the results agreed.

[1]G. Sciaini and R. J. D. Miller, Rep. Prog. Phys. **74**, 096101 (2011).
[2]T. Elsaesser and M. Woerner, Acta Crystallogr., Sect. A: Found. Crystallogr. **66**, 168 (2010).
[3]S. Johnson, P. Beaud, C. Milne, F. Krasniqi, E. Zijlstra, M. Garcia, M. Kaiser, D. Grolimund, R. Abela, and G. Ingold, Phys. Rev. Lett. **100**, 155501 (2008).
[4]D. M. Fritz, D. A. Reis, B. Adams, R. A. Akre, J. Arthur, C. Blome, P. H. Bucksbaum, A. L. Cavalieri, S. Engemann, S. Fahy, R. W. Falcone, P. H. Fuoss, K. J. Gaffney, M. J. George, J. Hajdu, M. P. Hertlein, P. B. Hillyard, M. Horn-von Hoegen, M. Kammler, J. Kaspar, R. Kienberger, P. Krejcik, S. H. Lee, A. M. Lindenberg, B. McFarland, D. Meyer, T. Montagne, E. D. Murray, A. J. Nelson, M. Nicoul, R. Pahl, J. Rudati, H. Schlarb, D. P. Siddons, K. Sokolowski-Tinten, T. Tschentscher, D. von der Linde, and J. B. Hastings, Science (N.Y.) **315**, 633 (2007).
[5]H. Ihee, V. A. Lobastov, U. M. Gomez, B. M. Goodson, R. Srinivasan, C. Y. Ruan, and A. H. Zewail, Science (N.Y.) **291**, 458 (2001).
[6]J. S. Kim, T. Lagrange, B. W. Reed, M. L. Taheri, M. R. Armstrong, W. E. King, N. D. Browning, and G. H. Campbell, Science (N.Y.) **321**, 1472 (2008).
[7]A. H. Zewail, Science (N.Y.) **328**, 187 (2010).
[8]O.-H. Kwon and A. H. Zewail, Science (N.Y.) **328**, 1668 (2010).
[9]J. R. Dwyer, C. T. Hebeisen, R. Ernstorfer, M. Harb, V. B. Deyirmenjian, R. E. Jordan, and R. J. D. Miller, Philos. Trans. R. Soc. London, Ser. A **364**, 741 (2006).
[10]B. J. Siwick, J. R. Dwyer, R. E. Jordan, and R. J. D. Miller, J. Appl. Phys. **92**, 1643 (2002).
[11]T. van Oudheusden, P. Pasmans, S. van der Geer, M. de Loos, M. van der Wiel, and O. Luiten, Phys. Rev. Lett. **105**, 264801 (2010).
[12]M. Gao, H. Jean-Ruel, R. Cooney, J. Stampe, M. de Jong, M. Harb, G. Sciaini, G. Moriena, and R. J. D. Miller, Opt. Express **20**, 12048 (2012).
[13]E. Fill, L. Veisz, A. Apolonski, and F. Krausz, New J. Phys. **8**, 272 (2006).
[14]M. Aidelsburger, F. O. Kirchner, F. Krausz, and P. Baum, Proc. Natl. Acad. Sci. U.S.A. **107**, 19714 (2010).
[15]Y. Murooka, N. Naruse, S. Sakakihara, M. Ishimaru, J. Yang, and K. Tanimura, Appl. Phys. Lett. **98**, 251903 (2011).
[16]A. Janzen, B. Krenzer, O. Heinz, P. Zhou, D. Thien, A. Hanisch, F.-J. Meyer Zu Heringdorf, D. von der Linde, and M. Horn von Hoegen, Rev. Sci. Instrum. **78**, 013906 (2007).
[17]S. Schäfer, W. Liang, and A. H. Zewail, J. Chem. Phys. **135**, 214201 (2011).
[18]W. Liang, S. Schäfer, and A. H. Zewail, Chem. Phys. Lett. **542**, 1 (2012).

[19]P. Baum and A. H. Zewail, Proc. Natl. Acad. Sci. U.S.A. **103**, 16105 (2006).
[20]P. Hommelhoff, Y. Sortais, A. Aghajani-Talesh, and M. A. Kasevich, Phys. Rev. Lett. **96**, 077401 (2006).
[21]C. Ropers, D. R. Solli, C. P. Schulz, C. Lienau, and T. Elsaesser, Phys. Rev. Lett. **98**, 043907 (2007).
[22]B. Cho, T. Ichimura, R. Shimizu, and C. Oshima, Phys. Rev. Lett. **92**, 246103 (2004).
[23]B. Barwick, C. Corder, J. Strohaber, N. Chandler-Smith, C. Uiterwaal, and H. Batelaan, New J. Phys. **9**, 142 (2007).
[24]H. Yanagisawa, C. Hafner, P. Doná, M. Klöckner, D. Leuenberger, T. Greber, M. Hengsberger, and J. Osterwalder, Phys. Rev. Lett. **103**, 257603 (2009).
[25]H. Yanagisawa, C. Hafner, P. Doná, M. Klöckner, D. Leuenberger, T. Greber, J. Osterwalder, and M. Hengsberger, Phys. Rev. B **81**, 115429 (2010).
[26]H. Yanagisawa, M. Hengsberger, D. Leuenberger, M. Klöckner, C. Hafner, T. Greber, and J. Osterwalder, Phys. Rev. Lett. **107**, 087601 (2011).
[27]M. Schenk, M. Krüger, and P. Hommelhoff, Phys. Rev. Lett. **105**, 257601 (2010).
[28]M. Krüger, M. Schenk, and P. Hommelhoff, Nature **475**, 78 (2011).
[29]P. Hommelhoff, C. Kealhofer, and M. A. Kasevich, Phys. Rev. Lett. **97**, 247402 (2006).
[30]R. Bormann, M. Gulde, A. Weismann, S. Yalunin, and C. Ropers, Phys. Rev. Lett. **105**, 147601 (2010).
[31]G. Herink, D. R. Solli, M. Gulde, and C. Ropers, Nature **483**, 190 (2012).
[32]L. V. Keldysh, Sov. Phys. JETP **20**, 1307 (1965).
[33]Y. C. Martin, H. F. Hamann, and H. K. Wickramasinghe, J. Appl. Phys. **89**, 5774 (2001).
[34]C. Hebeisen, G. Sciaini, and M. Harb, Opt. Express **16**, 3334 (2008).
[35]T. van Oudheusden, E. F. de Jong, S. B. van der Geer, W. P. E. M. Op t Root, O. J. Luiten, and B. J. Siwick, J. Appl. Phys. **102**, 093501 (2007).
[36]M. Germann, T. Latychevskaia, C. Escher, and H.-W. Fink, Phys. Rev. Lett. **104**, 095501 (2010).
[37]L. Reimer and H. Kohl, *Transmission Electron Microscopy: Physics of Image Formation* (Springer Verlag, Berlin, 2008).
[38]R. Gomer, *Field Emission and Field Ionization* (Harvard University Press, Cambridge, MA, USA, 1961).
[39]We tested angular distributions of the initial velocity at each emission spot but found the effects to be small compared to the emission site dependence.
[40]For Gaussian shape of the distribution $\tau(t)$, the FWHM is $\approx 2.35\ \sigma_\tau$.
[41]S. Hilbert, A. Neukirch, C. J. G. J. Uiterwaal, and H. Batelaan, J. Phys. B **42**, 141001 (2009).
[42]S. V. Yalunin, M. Gulde, and C. Ropers, Phys. Rev. B **84**, 195426 (2011).
[43]Here, the beam waist is defined according to a 2D spatial distribution similar to the definition of $\sigma_\tau$.
[44]We note that in cases where the lens is operated at large focal lengths, as, for example, in parallel beam diffraction with the focal point on a distant detector, the decelerating lens regimes can be favorable due to the interplay between lens-induced path length differences and velocity changes.
[45]C. Schwab, *p- and hp-Finite Element Methods: Theory and Applications to Solid and Fluid Mechanics* (Oxford University Press, 1998).
[46]R. Karrer, H. J. Neff, M. Hengsberger, T. Greber, and J. Osterwalder, Rev. Sci. Instrum. **72**, 4404 (2001).